

# Temperature evolution of lattice misfit in Hf and Mo variations of the $\text{Al}_{10}\text{Co}_{25}\text{Cr}_8\text{Fe}_{15}\text{Ni}_{36}\text{Ti}_6$ compositionally complex alloy

A.M. Manzoni<sup>1,2\*</sup>, S. Haas<sup>3</sup>, H. Kropf<sup>2</sup>, J. Duarte<sup>4</sup>, C. T Cakir<sup>1,2</sup>, F. Dubois<sup>2</sup>, D. Töbrens<sup>2</sup>, U. Glatzel<sup>3</sup>

\*Corresponding Author: [anna\\_manzoni@gmx.net](mailto:anna_manzoni@gmx.net)

<sup>1</sup>Bundesanstalt für Materialforschung und -prüfung, Unter den Eichen 87, D-12205 Berlin, Germany

<sup>2</sup>Helmholtz-Zentrum Berlin für Materialien und Energie GmbH, Hahn-Meitner-Platz 1, 14109 Berlin, Germany

<sup>3</sup>Metals and Alloys, University Bayreuth, Prof.-Rüdiger-Bormann-Str. 1, 95447 Bayreuth, Germany

<sup>4</sup>Max-Planck-Institut für Eisenforschung GmbH, Max-Planck-Straße 1, D- 40237 Düsseldorf

## Abstract

Misfits of  $\gamma$ - $\gamma'$  based  $\text{Al}_{10}\text{Co}_{25}\text{Cr}_8\text{Fe}_{15}\text{Ni}_{36}\text{Ti}_6$  and its Mo- and Hf-variations are studied up to a temperature of 980°C and compared with Ni- and Co-based superalloys. The trace elements decrease (Hf) or increase (Mo) the edge radii of the  $\gamma'$  cuboids without changing their sizes. Atom probe measurements revealed that the Hf alloy prefers the  $\gamma'$  phase while Mo prefers the  $\gamma$  matrix, leading to a lattice parameters enhancement of both phases, as could be revealed by synchrotron X-ray diffraction. The misfit is influenced in opposite ways: Hf increases the positive misfit, while Mo reduces it at all investigated temperatures.

**Keywords:** metal and alloys; transmission electron microscopy; X-ray diffraction; atom probe tomography; high entropy alloy

Multi-phase compositionally complex alloys (CCA) are alloys which rely on the high entropy concept, and in addition to the solid solution strengthening they use the strengthening potential of one or more secondary phases. A controlled introduction of a strengthening second phase, like e.g. in Ni-based superalloys, became an important subject of research in CCA, especially in case of possible high-temperature applications [1, 2].

In this study, such an alloy, i.e.  $\text{Al}_{10}\text{Co}_{25}\text{Cr}_8\text{Fe}_{15}\text{Ni}_{36}\text{Ti}_6$ , which has been introduced before [1, 3-7], will be the base for an optimization for higher temperature application at about 700°C, using two trace elements Mo and Hf, which are known for their beneficial properties in Ni-based superalloys [8].

A good overview over the room temperature microstructure and the mechanical properties at different temperatures of the  $\text{Al}_{10}\text{Co}_{25}\text{Cr}_8\text{Fe}_{15}\text{Ni}_{36}\text{Ti}_6$ ,  $\text{Al}_9\text{Co}_{25}\text{Cr}_8\text{Fe}_{15}\text{Ni}_{36}\text{Ti}_6\text{Mo}_1$ , and  $\text{Al}_{9.5}\text{Co}_{25}\text{Cr}_8\text{Fe}_{15}\text{Ni}_{36}\text{Ti}_6\text{Hf}_{0.5}$  alloys have been given in a previous work [3]. The alloys are characterized by a three-phase morphology, i.e. the  $\gamma$ - $\gamma'$  combination that is aimed for and a Heusler phase of  $\text{L}_{21}$  structure, and, in case of Hf, additional Hf-rich phases. An additional secondary  $\gamma'$  could be observed as well. A precise insight into the Heusler and secondary  $\gamma'$  phases has been given in [5].

However, no information has been gained yet on the evolution of the microstructure at higher temperatures, especially concerning the  $\gamma$ - $\gamma'$  morphology, that is known from superalloys to be crucial for the mechanical stability at high temperatures [8]. One important parameter for this stability is the lattice misfit between the coherent  $\gamma$  and  $\gamma'$  phases and especially its evolution over temperature. Depending on the composition, this misfit can be positive or negative. It has been suggested [9] that a positive misfit can imply a particularly interesting high temperature

behaviour. The base alloy shows a positive misfit at room temperature, as has been shown before [5], but the impact of Hf and Mo remains to be determined.

This work focuses thus on the influence on the lattice parameters that is induced by the introduction of the two trace elements Hf and Mo, the evolution of the alloys' misfits with temperature and an atom probe study about the trace elements' whereabouts in the alloy. Their large atomic radii ( $r_{\text{Hf}} = 0.158$  nm,  $r_{\text{Mo}} = 0.140$  nm) are expected to increase the lattice parameters of the phases into which they will diffuse. In order to gain this information, a combination of transmission electron microscopy (TEM), atom probe tomography (APT) and synchrotron X-ray diffraction is used on the three alloys.

The  $\text{Al}_{10}\text{Co}_{25}\text{Cr}_8\text{Fe}_{15}\text{Ni}_{36}\text{Ti}_6$  (base alloy),  $\text{Al}_9\text{Co}_{25}\text{Cr}_8\text{Fe}_{15}\text{Ni}_{36}\text{Ti}_6\text{Mo}_1$  (Mo-alloy), and  $\text{Al}_{9.5}\text{Co}_{25}\text{Cr}_8\text{Fe}_{15}\text{Ni}_{36}\text{Ti}_6\text{Hf}_{0.5}$  (Hf-alloy) CCA were prepared from constituent elements with 99.99% purity. They were cast in a vacuum induction furnace. Sample homogenization was carried out at 1220°C for 20 h in case of the  $\text{Al}_{10}\text{Co}_{25}\text{Cr}_8\text{Fe}_{15}\text{Ni}_{36}\text{Ti}_6$  and  $\text{Al}_9\text{Co}_{25}\text{Cr}_8\text{Fe}_{15}\text{Ni}_{36}\text{Ti}_6\text{Mo}_1$  alloys and at 1130°C for 20 h in case of the  $\text{Al}_{9.5}\text{Co}_{25}\text{Cr}_8\text{Fe}_{15}\text{Ni}_{36}\text{Ti}_6\text{Hf}_{0.5}$  alloy, with a subsequent cooling in the furnace. The homogenized samples were then aged at 900°C for 50 h (base and Hf-alloy) of 100 h (Mo-alloy) and cooled inside the furnace. The Mo-alloy used for APT measurement was aged at 900°C for 50 h, which has no influence on the Mo's segregation towards a specific phase.

Samples for optical microscopy, SEM and synchrotron measurements were ground and polished mechanically, down to a final polishing step with a 50 nm sized colloidal silica suspension. Some samples for SEM were etched for better contrast, using an etching solution of 50 ml  $\text{H}_2\text{O}$ , 50 ml  $\text{HCl}$ , 50 ml  $\text{HNO}_3$  and 1.5 g  $\text{H}_2\text{MoO}_4$ .

Samples for synchrotron measurements were oriented in a home-built Laue diffractometer operating with a Tungsten x-ray tube operating at 25 kV. Data are recorded on a  $12 \times 12$  cm<sup>2</sup> sized image plate which is read out with a pixel size of 100  $\mu\text{m}$ . Data was analyzed with the OrientExpress software [10].

Atom probe tomography samples were prepared in two different ways: the Hf-alloy was cut to rods of  $0.25 \times 0.25 \times 10$  mm<sup>3</sup> size and APT tips were prepared via electropolishing in two steps with a final polishing solution of 98% butoxyethanol and 2% perchloric acid and a final voltage of 3 V. The Mo-alloy was prepared in a Zeiss FIB Crossbeam<sup>®</sup> 1540 at HZB by mounting sample pieces onto tips on a Si coupon provided by CAMECA. The final thinning down to ~50 nm tip radius was realized in an FEI FIB Helios dual beam at MPIE by an annular milling tool.

The TEM used in this work was a Philips CM30, operated at 300 kV. TEM specimens mechanically polished to a thickness of 140  $\mu\text{m}$  and then electropolished with a polishing solution of 83% ethanol, 10% perchloric acid and 7% glycerine at -7°C and a voltage of 30 V.

Atom probe measurements were carried out in two different atom probes: the Hf-alloy was measured in a LEAP3000 by CAMECA at a pulse rate of 200 000 Hz, at a temperature of 60 K and 15 % pulse fraction. The Mo-alloy was measured in a LEAP5000HR by CAMECA, at a pulse rate of 150 000 Hz (because 200 000 Hz was too high), at a temperature of 60 K and 15 % pulse fraction. Data was reconstructed using IVAS 3.8 and analyzed using IVAS 3.6.12. Concentration profiles were acquired along a cylinder of 4 nm in diameter, using a fixed sample count of 400 ions and 240 ions per step. All bulk concentrations given in this work are an average over 10 cubes of  $5 \times 5 \times 5$  nm<sup>3</sup> sized cubes, that were randomly distributed through the corresponding phase in the tip (primary  $\gamma'$  and  $\gamma$ ) or by setting an iso-concentration surface of Cr at 4 at.% and measuring the bulk concentration of the 10 largest precipitates (secondary  $\gamma'$ ).

Synchrotron diffraction data were collected at the KMC-2 beamline [11] at BESSY II in Berlin, Germany, using a monochromatic radiation of 8048 eV energy, which corresponds to the Cu  $K\alpha_1$  wavelength (0.15406 nm). The beam size was  $0.5 \times 0.5 \text{ mm}^2$ . An xy-translation table allowed for locating the sample regions that were previously determined and marked by Laue diffraction. Samples were mounted on a heating plate and covered with a beryllium dome to provide an ultra-high vacuum of  $10^{-6}$  mbar at several temperatures (200, 830, 880, and  $930^\circ\text{C}$ ) up to  $980^\circ\text{C}$ , if possible. The configuration at KMC-2 corresponds to a classic  $\theta$ - $2\theta$  geometry and the setup and the data acquisition have been described in a previous work [5]. The measured reflexes were 100 and 200 for the base and Mo-alloy and 110 and 220 for the Hf-alloy. 100 and 110 peaks were used only for determining the sign of the misfit. The experimental optimum value for all peak intensities was determined by tilting the position of the sample in the  $\theta$ - $2\theta$  plane by an angle of  $\Delta\eta \approx 0.5^\circ$  around the optimum Bragg angle. Finally, the lattice parameters for  $\gamma$  and  $\gamma'$  were calculated by taking the average of all peak positions for the different  $\eta$  values. The Origin<sup>®</sup> software [12] was used for peak fitting.

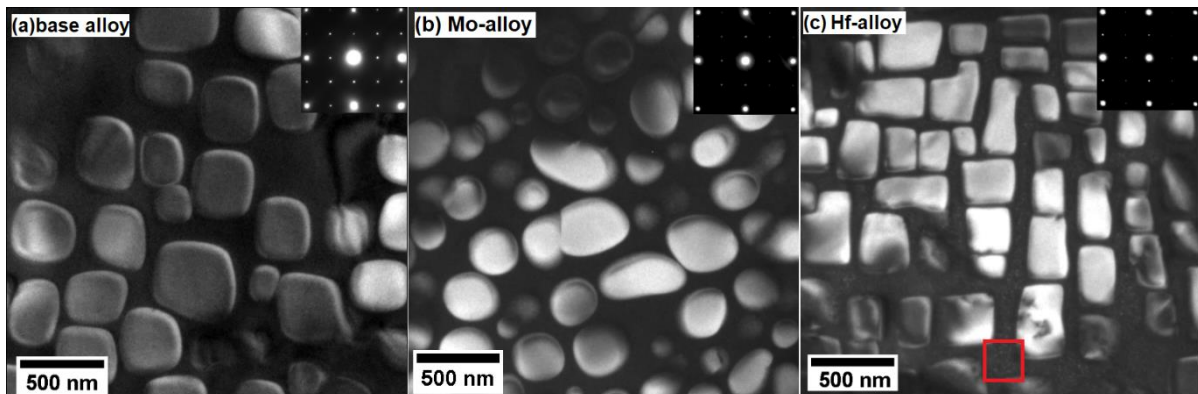


Figure 1: TEM DF micrographs of the  $\gamma/\gamma'$  morphology in the (a)  $\text{Al}_{10}\text{Co}_{25}\text{Cr}_8\text{Fe}_{15}\text{Ni}_{36}\text{Ti}_6$ , (b)  $\text{Al}_9\text{Co}_{25}\text{Cr}_8\text{Fe}_{15}\text{Ni}_{36}\text{Ti}_6\text{Mo}_1$ , and (c)  $\text{Al}_{9.5}\text{Co}_{25}\text{Cr}_8\text{Fe}_{15}\text{Ni}_{36}\text{Ti}_6\text{Hf}_{0.5}$  alloys and the corresponding SAD in the upper right corner. All images have been taken along the [001] zone axis and imaged with the (110) diffraction spot. The red square highlights a region where the secondary  $\gamma'$  particles are best visible.

Figure 1 shows the  $\gamma/\gamma'$  morphology in the (a)  $\text{Al}_{10}\text{Co}_{25}\text{Cr}_8\text{Fe}_{15}\text{Ni}_{36}\text{Ti}_6$ , (b)  $\text{Al}_9\text{Co}_{25}\text{Cr}_8\text{Fe}_{15}\text{Ni}_{36}\text{Ti}_6\text{Mo}_1$ , and (c)  $\text{Al}_{9.5}\text{Co}_{25}\text{Cr}_8\text{Fe}_{15}\text{Ni}_{36}\text{Ti}_6\text{Hf}_{0.5}$  alloys, as visualized with TEM DF along the [001] zone axis with the 110 diffraction spot. The corresponding SAD is given in the upper right corner. The secondary  $\gamma'$  precipitates can be observed in all three alloys but are best visible in the highlighted red box in (c). Their formation has been described in detail in [5] and they will only play a minor role in this work. Note that the horizontal and vertical  $\gamma$  channels, playing a major role in  $\gamma'$  enriched alloys such as CMSX-4 [13], will not be treated separately in the following as it can be assumed from their width that no major tetragonal distortion of the  $\gamma$  unit cell is to be expected."

While the size of the primary  $\gamma'$  precipitates is hardly modified [3], their shape changes remarkably with the trace element. The cuboid precipitates in the base alloy turn quite spherical in the alloy with Mo (b) and acquire much sharper edges, i.e. smaller edge radii, when Hf is added (c). A comparison of their volume fractions has been given in [3]:  $38 \pm 7 \text{ vol. } \%$   $\gamma'$  in the base alloy,  $44 \pm 1 \text{ vol. } \%$   $\gamma'$  in the Mo-alloy and  $46 \pm 2 \text{ vol. } \%$   $\gamma'$  in the Hf-alloy.

It is known from Ni-based superalloys that the shape of the  $\gamma'$  phase is directly linked to the lattice misfit between the  $\gamma$  and  $\gamma'$  phase [8]. The magnitude of this misfit and its chemical origin shall be determined in the following.

In order to determine the chemical composition of the  $\gamma$  and  $\gamma'$  phases, three-dimensional atom probe was used. Figure 2 shows the three-dimensional reconstructions of a) the Hf- and b) the Mo-alloys. They highlight 30% of the Co and Fe atoms and the iso-concentration surfaces set at 5 at.% Cr, in green colour. On the lower left side both reconstructions hit a primary  $\gamma'$  particle. The other smaller particles are secondary  $\gamma'$ . Qualitative preview concentration profiles have been taken along cylinders of 1 nm in diameter (shown in red) that truncate the primary and secondary  $\gamma'$  particles. The 1D preview concentration depth profiles qualitatively show the enrichment in Ni, Al and Ti in the  $\gamma'$  particles and an enrichment in Fe, Cr and Co in the  $\gamma$  matrix, as had already been determined in the base alloy before [5]. Because of the low concentrations of the trace elements, a zoom on the elements with lowest percentage, i.e. Ti and Hf/Mo, is shown in extra graphs. An increase in Hf concentration can be seen inside the primary and the secondary  $\gamma'$  phase, while an increase in Mo can be observed in the  $\gamma$  matrix.

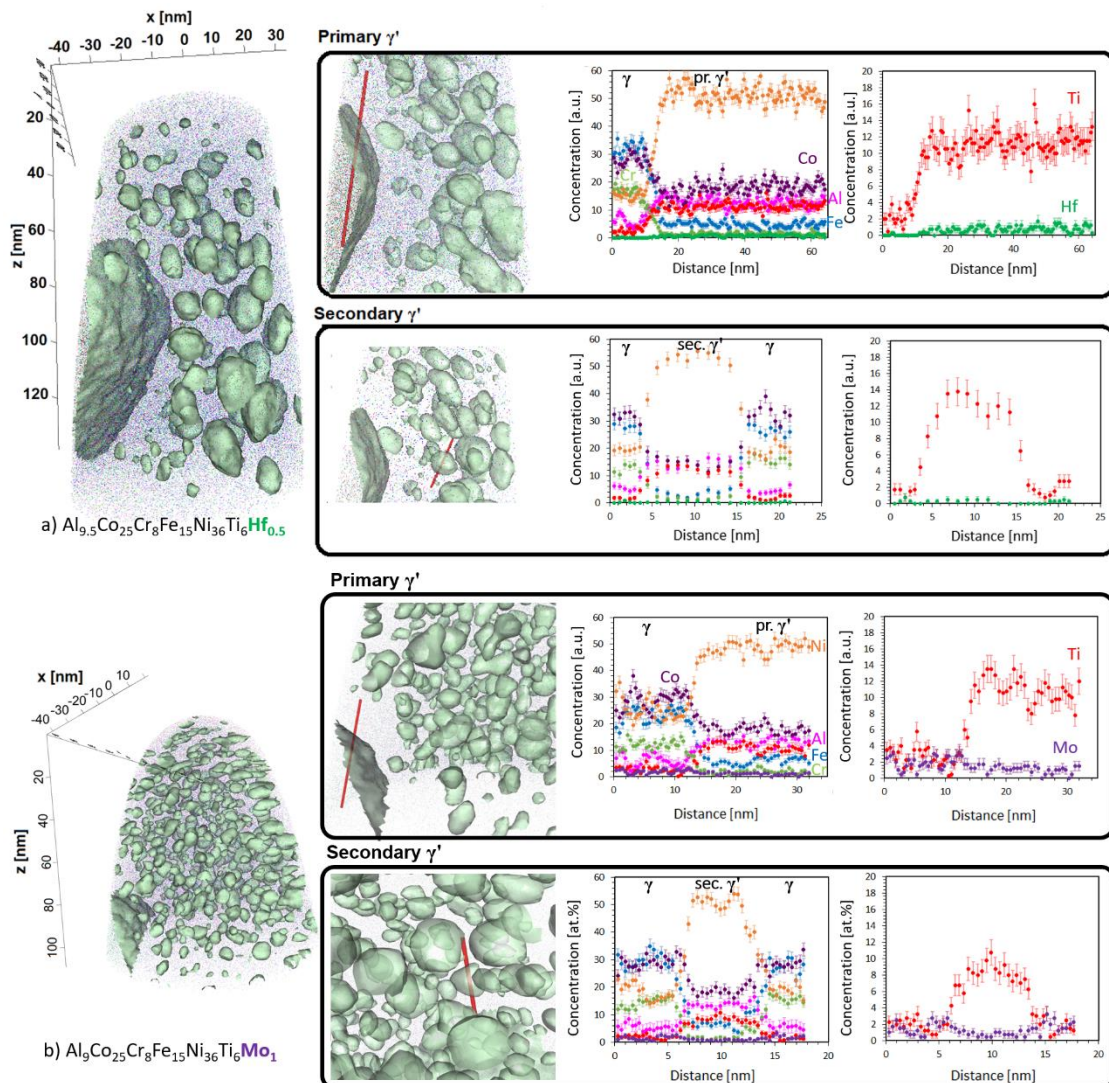


Figure 2: APT data on a) the  $\text{Al}_{9.5}\text{Co}_{25}\text{Cr}_8\text{Fe}_{15}\text{Ni}_{36}\text{Ti}_6\text{Hf}_{0.5}$  alloy and b) the  $\text{Al}_9\text{Co}_{25}\text{Cr}_8\text{Fe}_{15}\text{Ni}_{36}\text{Ti}_6\text{Mo}_1$  alloy: 3D reconstruction of volume of about  $100\text{-}120 \times 70 \times 70 \text{ nm}^3$  (in green: Cr iso-concentration surfaces at 5 at.%), a zoom on the particles and the positions of the cylinders along which the concentration depth profiles have been taken (in red), the concentration depth profiles taken along the cylinders, and a zoom of the latter on the Ti and Hf/Mo elements.

As the shown concentration profiles only give information on one particle, quantitative information was gained statistically using different regions of interest (ROI) and averaging over the whole dataset. All concentrations of all investigated phases in the two alloys have been

summarized in Table 1, along with the standard deviation, and completed with data of the base alloy from a previous work for comparison [5].

Alloy	Phase	Concentration [at.%]								Ref. / note
		Al	Co	Cr	Fe	Ni	Ti	Mo	Hf	
Al <sub>10</sub> Co <sub>25</sub> Cr <sub>8</sub> Fe <sub>15</sub> Ni <sub>36</sub> Ti <sub>6</sub>	nominal	10	25	8	15	36	6	-	-	
	$\gamma$	4.9 ± 0.1	<b>28.0</b> ± 0.1	11.2 ± 0.1	<b>22.6</b> ± 0.2	31.2 ± 0.1	1.5 ± 0.1	-	-	[5]
	$\gamma'$ pr.	<b>11.4</b> ± 0.6	22.5 ± 0.6	3.5 ± 0.4	8.8 ± 0.7	<b>45.0</b> ± 1.5	<b>8.7</b> ± 0.5	-	-	[5]/ TEM – EDS data
	$\gamma'$ sec.	<b>14.3</b> ± 0.8	20.6 ± 0.9	1.5 ± 0.2	4.7 ± 0.9	<b>48.8</b> ± 1.1	<b>9.8</b> ± 0.7	-	-	[5]
	nominal	9	25	8	15	36	6	1	-	
Al <sub>9</sub> Co <sub>25</sub> Cr <sub>8</sub> Fe <sub>15</sub> Ni <sub>36</sub> Ti <sub>6</sub> Mo <sub>1</sub>	$\gamma$	6.2 ± 0.6	<b>28.5</b> ± 1.2	<b>13.3</b> ± 1.6	<b>25.1</b> ± 1.4	22.3 ± 2.3	2.6 ± 0.4	<b>1.7</b> ± 0.3	-	This work
	$\gamma'$ pr.	<b>12.6</b> ± 0.5	18.7 ± 1.2	2.0 ± 0.2	6.3 ± 0.4	<b>48.0</b> ± 0.6	<b>11.4</b> ± 0.5	0.8 ± 0.1	-	This work
	$\gamma'$ sec.	<b>13.6</b> ± 0.8	17.2 ± 0.9	1.5 ± 0.2	5.1 ± 0.5	<b>50.1</b> ± 1.0	<b>10.6</b> ± 0.8	1.0 ± 0.2	-	This work
Al <sub>9.5</sub> Co <sub>25</sub> Cr <sub>8</sub> Fe <sub>15</sub> Ni <sub>36</sub> Ti <sub>6</sub> Hf <sub>0.5</sub>	nominal	9.5	25	8	15	36	6	-	0.5	
	$\gamma$	<b>5.0</b> ± 0.5	31.5 ± 1.4	13.9 ± 0.9	27.6 ± 0.9	<b>20.1</b> ± 0.7	<b>1.7</b> ± 0.4	-	<b>0.1</b> ± 0.0	This work
	$\gamma'$ pr.	<b>12.4</b> ± 0.6	17.9 ± 1.0	1.4 ± 0.2	4.7 ± 0.6	<b>51.9</b> ± 1.1	<b>11.0</b> ± 0.9	-	<b>0.7</b> ± 0.1	This work
	$\gamma'$ sec.	<b>14.8</b> ± 0.3	15.0 ± 0.7	1.1 ± 0.1	3.9 ± 0.4	<b>53.5</b> ± 1.2	<b>11.5</b> ± 0.5	-	<b>0.2</b> ± 0.1	This work

Table 1: Chemical composition of the  $\gamma$ , primary and secondary  $\gamma'$  in Al<sub>9</sub>Co<sub>25</sub>Cr<sub>8</sub>Fe<sub>15</sub>Ni<sub>36</sub>Ti<sub>6</sub>Mo<sub>1</sub> and Al<sub>9.5</sub>Co<sub>25</sub>Cr<sub>8</sub>Fe<sub>15</sub>Ni<sub>36</sub>Ti<sub>6</sub>Hf<sub>0.5</sub> as determined by APT. Data on Al<sub>10</sub>Co<sub>25</sub>Cr<sub>8</sub>Fe<sub>15</sub>Ni<sub>36</sub>Ti<sub>6</sub> from [5] serves as a reference. The error bar is given by the standard deviation  $2\sigma$ . **Bold** numbers highlight the elements with the highest composition in this phase.

The qualitative insights from Figure 2 are confirmed in Table 1: Hf generally prefers to diffuse into the  $\gamma'$  phase, ( $0.7 \pm 0.1$  at.% vs.  $0.1 \pm 0.0$  at.% in  $\gamma$ ), even in the small secondary  $\gamma'$  precipitates ( $0.2 \pm 0.1$  at.%), and Mo prefers the  $\gamma$  matrix ( $1.7 \pm 0.3$  at.% vs.  $0.8 \pm 0.1$  or  $1.0 \pm 0.2$  at.% in primary and secondary  $\gamma'$ , respectively). This is an observation that is also known from Ni-base superalloys: Hf is a classic  $\gamma'$  strengthener, diffusing mainly into the  $\gamma'$  phase and increasing its lattice parameter to a higher extent than it does in  $\gamma$ . At the same time, the opposite is true for Mo: Mo is a classic  $\gamma$  strengthener. It diffuses more into the  $\gamma$  phase and increases its lattice parameter, more than that of  $\gamma'$  [8].

In order to verify this expected behaviour, it is necessary to measure the lattice parameters of the two phases with a method that allows for the separation of the two phases.

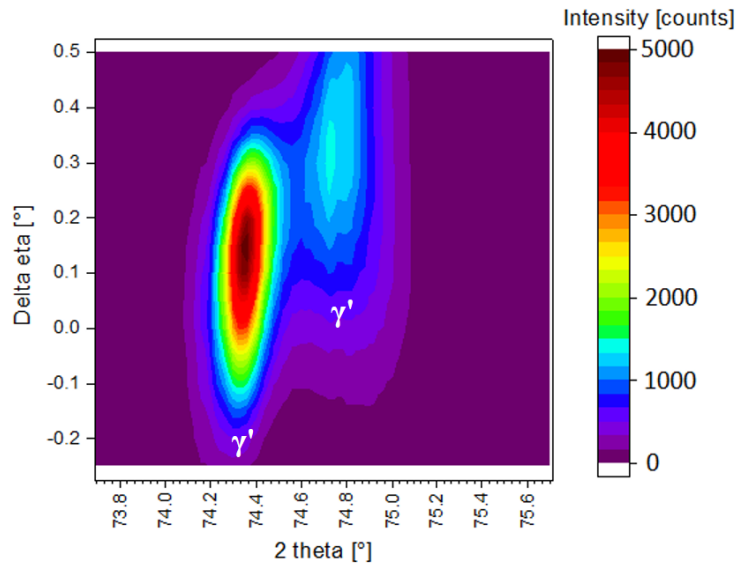


Figure 3: Heat map of the combined synchrotron diffractograms of  $\text{Al}_{9.5}\text{Co}_{25}\text{Cr}_8\text{Fe}_{15}\text{Ni}_{36}\text{Ti}_6\text{Hf}_{0.5}$  in the region around  $2\theta=74.5^\circ$  (220 peaks). The y axis  $\Delta\eta$  corresponds to the angular distance from the optimum value for  $\eta$ .

Figure 3 exemplarily shows the heat map of the  $\gamma$  and  $\gamma'$  peaks at room temperature recorded at the KMC-2 beamline around  $\sim 74.5^\circ$  for the 220 peaks in the Hf-alloy. The  $\gamma'$  peak is positioned at lower  $2\theta$  values, as could be verified by recording the 100 or 110 peaks and calculating the lattice parameter (not shown here).

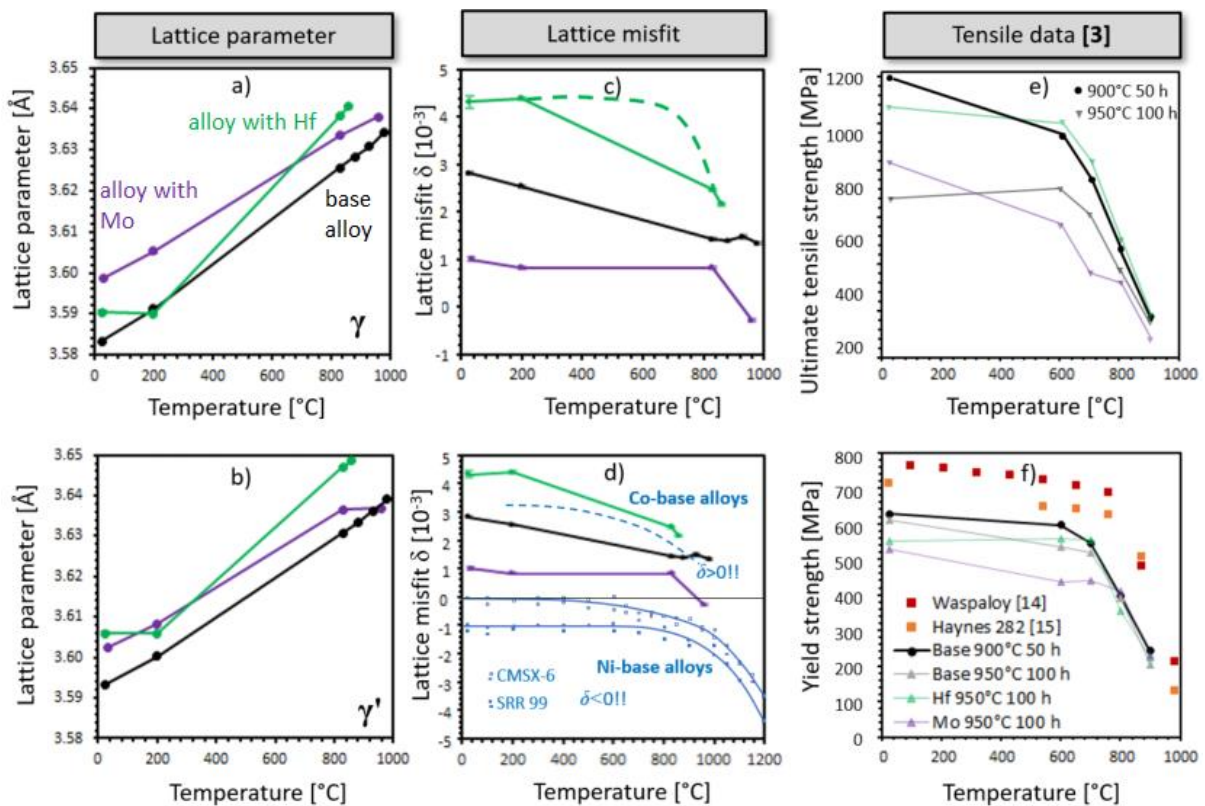


Figure 4: Evolution with temperature of (a) the lattice parameters in  $\gamma$ ; (b) the lattice parameters in  $\gamma'$ ; (c) the lattice misfit in the  $\text{Al}_{10}\text{Co}_{25}\text{Cr}_8\text{Fe}_{15}\text{Ni}_{36}\text{Ti}_6$  alloy and the variations with Mo and Hf; (d) the misfit integrated into Mughrabi's qualitative schematic on positive and negative misfit in superalloys, adapted from [9]; ultimate tensile strength of the three directionally solidified alloys (semi-transparent data: after annealing at  $950^\circ\text{C}$  100 h), as reported in and adapted from [3]; and yield strength of the three directionally solidified alloys (semi-transparent data: after annealing at  $950^\circ\text{C}$  100 h), as reported in and adapted from [3].

transparent data: after annealing at 950°C 100 h), as reported in and adapted from [3]. Data for Waspaloy [14] and Haynes 282 [15] for comparison. Error bars in synchrotron data correspond to the fitting errors and are in the order of  $10^{-4}$  -  $10^{-5}$ , thus mostly not visible.

Finally, Figure 4a and b show the temperature evolution of the lattice parameters of both phases, i.e. (a)  $\gamma$  and (b)  $\gamma'$ . Figure 4c reveals the lattice misfit as determined by using a fitting function of two Gaussian peaks, calculated according to [8]:

$$\delta = \frac{a_{\gamma'} - a_{\gamma}}{\frac{a_{\gamma} + a_{\gamma'}}{2}} \quad (\text{eq.1})$$

Both lattice parameters increase with temperature, as expected. In both phases and in both Mo- and Hf-alloys, the parameters are higher than in the base alloy. This means that even though Hf and Mo have their preferred phases (i.e.  $\gamma'$  and  $\gamma$ , respectively), they also diffuse to the other phase, increasing its parameter as well.

The lattice misfit at room temperature is positive in all three alloys, highest in case of the Hf-alloy ( $4.3 \times 10^{-3}$ ),  $2.8 \times 10^{-3}$  in case of the base alloy and lowest ( $1.5 \times 10^{-3}$ ) in case of the Mo-alloy. Fluctuations at high temperature are linked to the extremely small differences in values for the two phases  $\gamma$  and  $\gamma'$ . The lattice misfit decreases with the temperature, as is known from Ni- and Co-based alloys, shown in Figure 4d (adapted from [9]). In this work, Mughrabi showed the importance of sign and magnitude of the misfit on the expected mechanical properties. He expected the positive misfit to be an important factor (among others) to be beneficial for a high temperature application of the alloy.

Indeed the temperature and element evolution of the lattice misfit fit well with mechanical data determined in an earlier work [3]. Figure 4e and f show an adaptation of the ultimate tensile strength (UTS) and the yield strength (YS) results, respectively, on directionally solidified alloys. The annealing parameters in Ref. [3] were slightly different, i.e. 950°C 100 h (shown in semi-transparent). Data from the base alloy annealed at 900°C 50 h (shown in pure black) revealed that these annealing parameters lead to better tensile results. However, even after bad annealing the general behaviour of the UTS and the YS is reflected in the misfit and vice versa. The higher misfit in the Hf-alloy leads to a higher UTS at all temperatures, while the opposite is true for the Mo-alloy (except for room temperature). Similar conclusions can be drawn for the YS. Both misfit and strength decrease beyond 600°C. The misfit evolution between 200 and 830°C can only be guessed, however. The dashed line in case of the Hf-alloy shows the uppermost possible misfit evolution. Note also both the lattice misfit and the YS in the Hf-alloy increase from room temperature to the first temperature measurement (200°C or 600°C, respectively). The reason for this is still unclear. It is expected that the values for UTS and YS are even higher after improved annealing, i.e. at 900°C 50 h. Comparison of the three CCA's YS with that of commercial superalloys (Figure 4f) shows promising results for future optimization.

The work was supported by the DFG (German Research foundation) [grants WA 1378/15-2, GL 181/25-2, MA 7004/1-1 and -2, and GL 181/50-1 and -2].

We thank HZB for the allocation of synchrotron radiation beamtime at beamline KMC-2.

Many thanks to Konrad Siemensmeyer for help with Laue experiments and the Laue Camera at the HZB Quantum Material Core Lab; to Claudia Leistner for help with casting and heat treatment; to Christiane Förster for help with sample preparation; to Uwe Tezins for help with atom probe measurements; to M. Osenberg for fruitful discussion.

- [1] H.M. Daoud, A.M. Manzoni, N. Wanderka, U. Glatzel, *JOM* 67 (2015) 2271–2277.
- [2] J.Y. He, H. Wang, H.L. Huang, X.D. Xu, M.W. Chen, Y. Wu, X.J. Liu, T.G. Nieh, K. An, Z.P. Lu, *Acta. Mater.* 102 (2016) 187-196.
- [3] S. Haas, A.M. Manzoni, F. Krieg, U. Glatzel, *Entropy* 21(2) (2019) 169.
- [4] A. Manzoni, S. Haas, H. Daoud, U. Glatzel, C. Förster, N. Wanderka, *Entropy* 20(9) (2018) 646.
- [5] A.M. Manzoni, S. Haas, J.M. Yu, H.M. Daoud, U. Glatzel, H. Aboufadi, F. Mücklich, R. Duran, G. Schmitz, D.M. Többens, S. Matsumura, F. Vogel, N. Wanderka, *Mater. Char.* 154 (2019) 363-376.
- [6] A.M. Manzoni, S. Singh, H.M. Daoud, R. Popp, R. Völkl, U. Glatzel, N. Wanderka, *Entropy* 18(4) (2016) 104.
- [7] A.M. Manzoni, S. Singh, H.M. Daoud, R. Völkl, U. Glatzel, N. Wanderka, *The Jordan Journal of Physics* 8 (3) (2015) 177-186.
- [8] R.C. Reed, *The Superalloys. Fundamentals and Applications*, Cambridge University Press, Cambridge, 2006.
- [9] H. Mughrabi, *Acta. Mater.* 81 (2014) 21-29.
- [10] A. Filhol, J. Laugier, B. Bochu, The OrientExpress program for Laue indexing, <http://www.neutronoptics.com/OrientExpress.html>, ILL Grenoble, 1999.
- [11] *Journal of large-scale research facilities* 2 (2016) A49.
- [12] Origin(Pro), OriginLab Corporation, Northampton, MA, USA, 2017.
- [13] U. Glatzel, A. Muller, *Scripta Met. Mater.* 31(3) (1994) 285-290.
- [14] <https://www.specialmetals.com/assets/smc/documents/alloys/other/waspaloy.pdf>.
- [15] <http://haynesintl.com/docs/default-source/pdfs/new-alloy-brochures/high-temperature-alloys/brochures/282-brochure.pdf?sfvrsn=20>).